Visible light photocatalytic performance of Y-Fe co-doped with SrTiO₃ perovskite powder

Jing Wang, Nan Li, Yanhua Tang, Yunlong He, and Ke Shan[*]

College of Science, Honghe University, Yunnan Province 661199, China
[*]E-mail: shankekeshan@163.com

The Y and Fe doped SrTiO₃ compound photocatalytic material ($Y_{0.03}Sr_{0.97}Ti_{1-x}Fe_xO_{3-\delta}$ (x = 0.03, 0.04, 0.05)) was prepared by Sol-gel method, and the effects of different doped amounts of Fe ions (x=0.03, 0.04, 0.05) on the samples' characteristics were then systematically examined using several techniques. X-ray diffraction (XRD) results indicated the formation of a cubic perovskite structure in all the samples. In accordance with the increased doping amount, the diffraction peak shifted across a large angle. EDS spectra demonstrated the successful doping of both Y and Fe into the SrTiO₃ lattice. Scanning electron microscopy (SEM) analysis showed that both the particle size reduction and uniformity of the samples changed with increasing doping amount. The UV–vis diffuse reflectance spectra (DRS) showed that the visible light absorption of pure strontium titanate (STO) was negligible and approached zero. However, there were obvious absorption edges around 400-800 nm for all doped samples. Photoluminescence (PL) results showed both the decreased PL intensity and defective state resulted from the effects of doping materials on SrTiO₃. Photocatalytic analysis showed that in the doped samples, methyl orange (MO) exhibited an increased degradation rate under visible irradiation. When the doping content of Fe ions was 0.04 ($Y_{0.03}Sr_{0.97}Ti_{0.96}Fe_{0.04}O_{3-\delta}$), we noted perfect photocatalytic activity which was approximately 2.31 times greater than that of pure SrTiO₃ (85% versus 36%). These results well elucidate the photocatalytic performance mechanisms.

Keyword: Y-Fe co-doped, SrTiO3, Visible light, photocatalytic.

1. INTRODUCTION

Recent decades have seen rapidly increasing problems related to global environmental pollution and energy shortages [1-2]. Recent years have also seen the constant innovation in various areas of industrial technology, including those related to chemical, leather, and textile printing and dyeing industries. Unfortunately, advances in these areas have resulted in a large increase in dye wastewater emissions. Given this, it is unsurprising that pollution caused by such wastewater has

become a worsening problem [3-4]. This has also highlighted the very real need to seek new industrial wastewater treatment measures for environmental governance and drinking water safety.

When compared with traditional methods, photocatalytic technology applied to wastewater treatment allows for the effective elimination of many previous stable pollutants. Moreover, this approach is also environmentally friendly, has a low cost and uses easily accessible raw materials; as such, photocatalysis is an optimal method for use in environment [5-6] At present, main photocatalysts include oxynitrides, sulfides, metal oxides, and perovskite structure materials [6-7]. The perovskite-based structural materials have a cubic crystal structure with a formula of ABO_3. This particular structure has several beneficial properties, including variable electronic and crystal structures, easy transformation of oxygen and electrons, and photo-stability. Moreover, the band structure is excitable by visible light. Due to this constellation of properties, perovskite based materials have attracted research interest for their applicability as a photocatalyst [8-12]. In particular, strontium titanate (STO) has been an excellent perovskitebased photocatalyst, owing to its outstanding thermal and chemical stabilities coupled with its excellent optical properties. However, as a consequence of a broad band gap, the light absorption capability of STO has been restricted to the UV light range. Despite this, past work has found that doping modifications efficiently enlarge the visible light response range and reduce its electronhole recombination rate. Critically, these modifications have significantly improved its photocatalytic activity [6, 13-14].

In general, to replace the position of Sr^{2+} and Ti^{4+}, the impurity ion must have a similar electronegativity and ionic radius as both Sr^{2+} and Ti^{4+}. These include Na^{3+} [15], Ba^{2+} [16], and La^{3+} ions that can be doped on the A-site and can replace the Sr-site. Moreover, Fe^{3+} [17], Co^{3+} [18], Mn^{3+} [19], Ni^{3+} [20], and Al^{3+} [21] ions can be doped on the B-site and can replace the Ti-site. To this end, Zhang Qidi and colleagues [22] synthesized the nanopowders of Bi-doped $SrTiO_3$ with different doping amounts. When the doping amount of Bi was 3%, degradation efficiency of Bi-$SrTiO_3$ on RHB was 77% higher than that of pure $SrTiO_3$ under visible light. Similarly, Abdi and colleagues [23] synthesized La-Fe co-doped $SrTiO_3$. The co-doped material exhibited a 19-fold greater photocatalytic activity than that of pure $SrTiO_3$ (96% versus 5%) with 4 wt% of Fe-La-doped $SrTiO_3$ nanoparticles. However, reports regarding Y-Fe co-doped $SrTiO_3$ as visible light photocatalysts remain few.

In this paper, a visible light photocatalyst $Y_{0.03}Sr_{0.97}Ti_{1-x}Fe_xO_{3-\delta}$ (x = 0.03, 0.04, 0.05) was prepared by doping Y^{3+} and Fe^{3+} into the Sr- and Ti-site of $SrTiO_3$, respectively, and the effect of the amount of doped Fe on visible lightinduced photocatalytic activity was then investigated.

2. EXPERIMENTAL PROCEDURE

2.1 Preparation

$Sr(CH_3COO)_2 \cdot 2H_2O$ (99%), $Ti(CH_3CH_2CH_2CH_2O)_4$ (99%), Fe_2O_3 (99%), and Y_2O_3 (99%) were used as raw materials to prepare $Y_{0.03}Sr_{0.97}Ti_{1-x}Fe_xO_{3-\delta}$ (x = 0.03, 0.04, or 0.05) using the sol-gel method [24] The pure strontium titanate was denoted as STO. When Y doping amount was 0.03 and Y doping amount was 0.03, 0.04, and 0.05, the prepared samples were denoted as STO1, STO2 and STO3, respectively. With a volume ratio of 1:4, $Ti(CH_3CH_2CH_2CH_2O)_4$ was added to a mixture of

anhydrous ethanol and isopropanol based on the stoichiometry of $Y_{0.03}Sr_{0.97}Ti_{1-x}Fe_xO_{3-\delta}$. Next, $Sr(CH_3COO)_2 \cdot 2H_2O$ solution was mixed with Y_2O_3, Fe_2O_3, and $Ti(CH_3CH_2CH_2CH_2O)_4$, stirred for 30 min, settled for 24 h, and then dried at 60°C. The dried gel was then ground and heated at 900°C for 10 h. Finally, a fine powder was obtained for use in later experiments.

In conjunction with a Rigaku D/max-A X-ray diffractometer and Cu Kα radiation, X-ray power diffraction (XRD) was utilized for phase identification. SEM (Zeiss-Sigma300) with an energy dispersive spectrometer (EDS) (Samx) was used to characterize the morphology of the synthesized samples. The specific surface area was determined using a pore size analyzer (Mike ASAP 2460), and the required low temperature environment (77K) was achieved with liquid nitrogen. UV-Vis diffuse reflectance spectroscopy (DRS) was measured using a UV-visible spectrophotometer (UV-PE950) with a range of 200-800 nm and a spectral bandwidth of 2 nm. The band gap energy (Eg) of the samples was obtained according to Equation (1):

$$\alpha h\nu = A(h\nu - Eg)^n \qquad (1)$$

Where A, α, and $h\nu$ are a constant, the absorption coefficient, and the photon energy, respectively. Eg is obtained by extrapolating the linear portion of a plot of $(\alpha h\nu)^2$ versus hν (Tauc curve).

The photoluminescence spectroscopy analysis was conducted using a fluorescence spectrometer (HORIBA FluoroMax-4). The valence states were investigated using the XPS technique (Thermo Fisher Scientific K-Alpha).

Photocatalytic performance was investigated as follows: 0.01 g sample powder was homogeneously dispersed into 5 mg/L methyl orange solution, after which 5 ml hydrogen peroxide solution (30 wt%) was added. After 1 h, the solution was put in front of a visible light lamp and the samples were extracted each hour at specified time durations for a total of 6 times. At a specified time duration, 10 mL sample solution was centrifuged at 8000 rpm for 5 min, and the extracted sample powder was then analyzed by UV–vis spectrophotometer. The degradation degree (DR%) of MO was calculated according to Equation (2):

$$DR(\%) = \frac{C_0 - C_t}{C_0} \qquad (2)$$

Where, C_0 and C_t are initial MO concentration and MO concentration after the intended irradiation time, respectively.

3. RESULTS AND DISCUSSION

Figure 1 shows the XRD patterns of $Y_{0.03}Sr_{0.97}Ti_{1-x}Fe_xO_{3-\delta}$ (x = 0.03, 0.04, 0.05). All the indexed peaks in the XRD spectra are ascribed to the cubic perovskite phase, and all the sample peaks are consistent with those provided on the standard card (JCPDS No.35-0734). According to these results, Y and Fe were not observed in the XRD patterns, which may have been due to their low contents. Compared to pure STO, the (110), (111), (200), and (210) peak intensities of the doped samples were all weaker. Moreover, results indicated a shifting of both (110) and (200) peaks to higher angles, which indicated that both Y^{2+} and Fe^{2+} had entered their corresponding positions in the STO

lattice. In addition, with increasing doping amount, the diffraction peak notably shifted to the right, resulting in an increased θ angle. According to Equation (3), we concluded that the interplanar spacing (d) of $Y_{0.03}Sr_{0.97}Ti_{1-x}Fe_xO_{3-\delta}$ (x = 0.03, 0.04, 0.05) decreased with increasing amount of doped Fe. This result indicated that the crystal cell gradually became smaller with increasing amount of doped Fe. This result was likely due to the defects in the crystal lattice, which inhibited the growth of grains so that the grain size gradually decreased.

$$2d\sin\theta = n\lambda \qquad (3)$$

Where, θ is incident angle, d is interplanar spacing, λ is wavelength and n is order of reflection.

The tolerance factor (*t*) can be calculated by the average radii of the A-site cations (r_A), B-site cations (r_B), and oxygen ion (r_O). The cubic perovskite structure was maintained for $0.95 < t < 1.04$.

$$t = (r_A + r_O)/[\sqrt{2}(r_B + r_O)] \qquad (4)$$

According to Equation (4), the calculated tolerance factors of $Y_xSr_{1-x}Ti_{0.9}In_{0.1}O_{3-\delta}$ (x= 0.03, 0.05, 0.07) were 0.9992, 0.9984, and 0.9982, respectively, suggesting that the amount of doped Fe did not influence the formation of the cubic perovskite structure. With increasing doped Fe, the tolerance factor of $Y_{0.03}Sr_{0.97}Ti_{1-x}Fe_xO_{3-\delta}$ gradually deviated from 1, suggesting the distortion degree of the material's perovskite structure gradually increased.
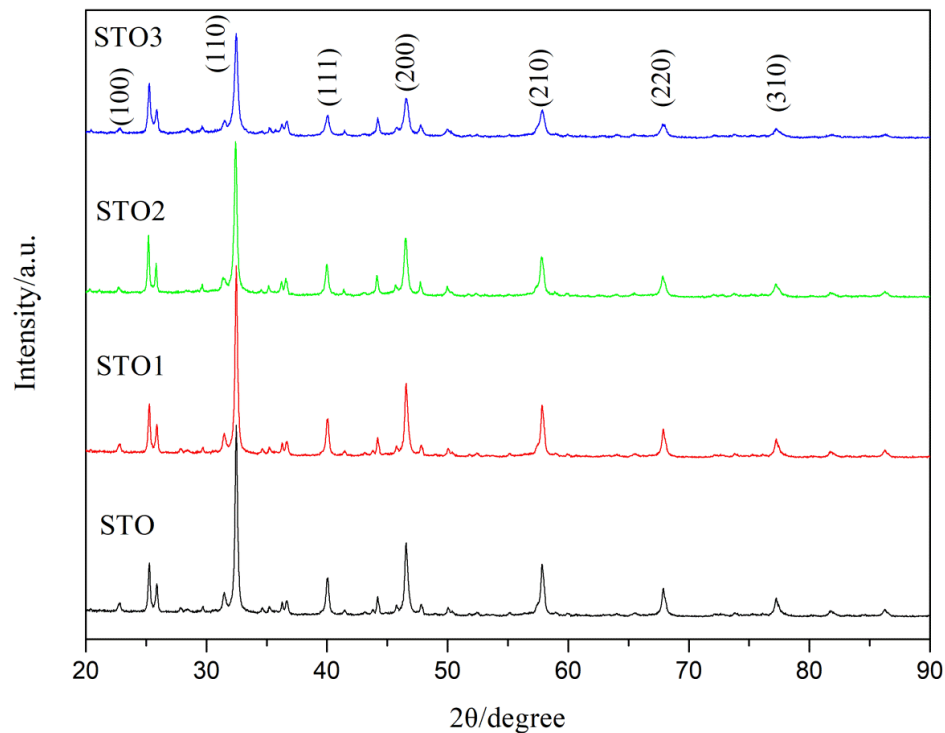
Figure 1. XRD patterns of $Y_{0.03}Sr_{0.97}Ti_{1-x}Fe_xO_{3-\delta}$ (x = 0.03, 0.04, 0.05) after sintering at 900°C for 6 h.

Figure 2 shows the SEM photographs of the fracture surfaces of $Y_{0.03}Sr_{0.97}Ti_{1-x}Fe_xO_{3-\delta}$ (x = 0.03, 0.04, 0.05). As shown in Figure 2, STO samples had STO aggregated grains and some apparent porosity. Moreover, the grains were not uniformly distributed. The particle size distribution became more homogeneous and the samples' particle size decreased with increasing doping elements. This may be due to defective crystal growth formed after doping. However, when the Fe^{3+} doping content increased to 0.05, the grains of samples increased again.
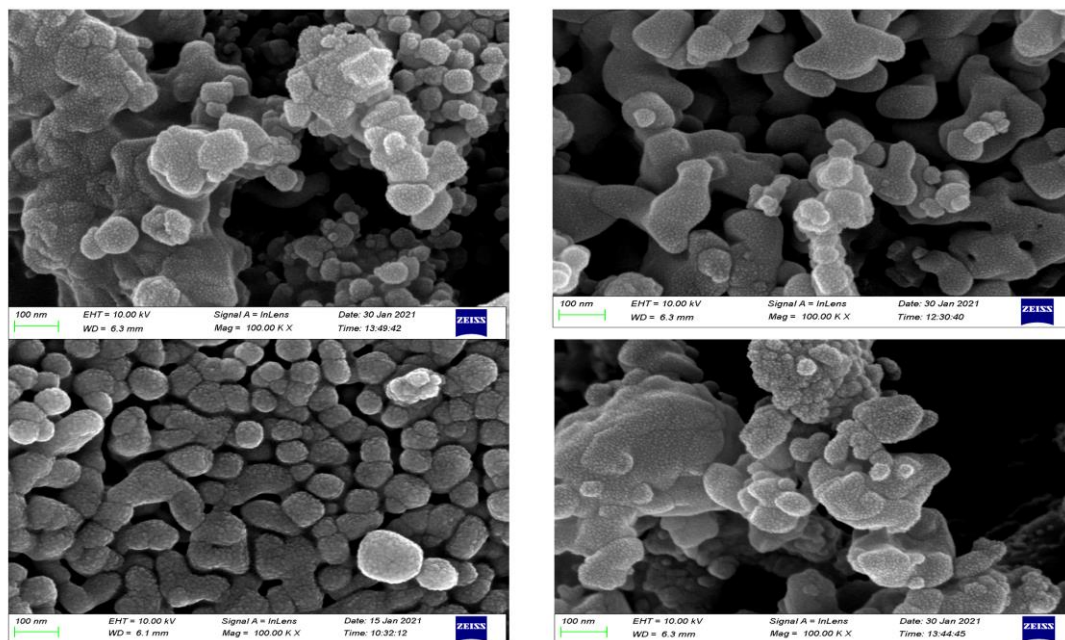

Figure 2. SEM micrographs of fracture surfaces of $Y_{0.03}Sr_{0.97}Ti_{1-x}Fe_xO_{3-\delta}$ (x=0.03, 0.04, 0.05) after sintering for 6 h at 900°C: (a) STO, (b) x=0.03, (c) x=0.04, (d) x=0.05.

The chemical compositions of the STO_2 nanoparticle samples were analyzed using microanalysis and EDS elemental mapping, and the results showed that O, Ti, and Sr were evenly distributed in the samples, indicating the formation of the STO perovskite structure. In addition, the doping process was demonstrated by the presence of Fe and Y in the EDS mapping of the STO_2 sample. The EDS spectra showed that the signals of Fe, Y, O, Sr, and Ti had no impurity peaks (Figure 3).

Figure 4 shows the N_2 adsorptiondesorption isotherms of STO and Y-Fe co-doped STO. From the indicated pattern, the adsorption amounts of pure STO and Y-Fe co-doped STO were less in the low pressure region, and when the relative pressure increased, the amount of adsorbed gas increased. All the samples showed a IV-type isotherm based on the Brunauer-Deming-Deming-Teller (BDDT) categorization. Moreover, an H3 type hysteresis loop appeared in the curves, which indicated that the nanoparticles in the samples had agglomerated and belonged to the mesoporous structure. The BET surface area of the Y-Fe co-doped STO was larger than that of the undoped samples, as shown in the inset.
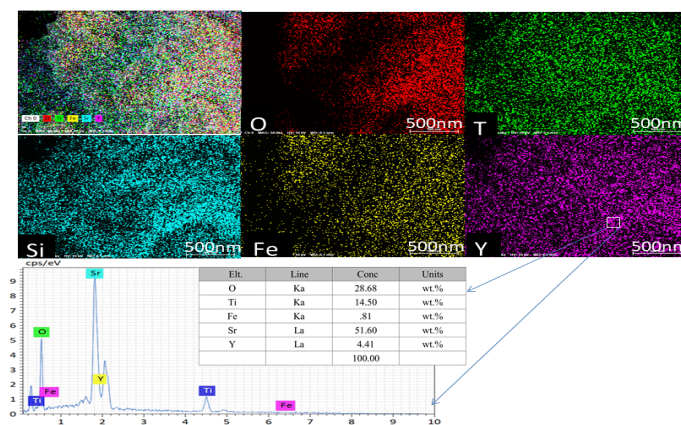
Figure 3. EDS microanalysis and EDS elemental mapping of the STO_2 sample.
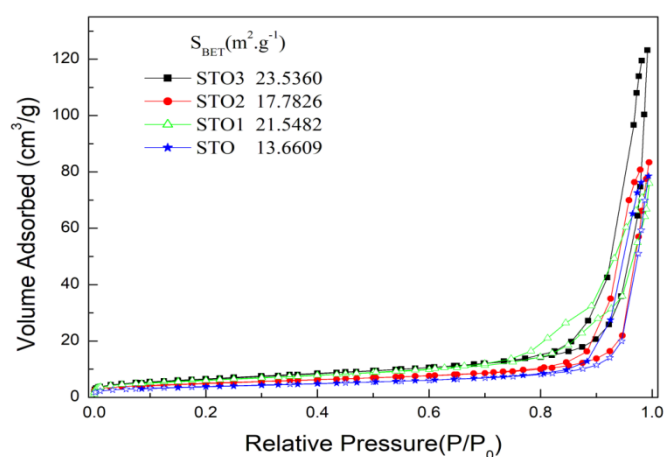
**Figure 4.** Nitrogen adsorption-desorption isotherms for all samples.

The photocatalytic activity of the Y-Fe co-doped STO was investigated next. PL spectroscopy was applied to explore the electronic structure as well as recombination and/or migration of the electron-hole pairs of the catalyst. The PL spectra of STO, STO_2, and STO_3 with an excitation wavelength of 320 nm at room temperature are shown in Figure 5. According to the spectra presented and when compared with the doped sample, pure STO had the strongest emission peak along with the largest peak area, suggesting that light conditions, the photogenerated electrons and holes are easy to recombine. The peak areas and intensities decreased with increasing doped Fe. This was largely due to point defects in the crystals that had been caused by Fe doping. This then produced a capture trap for the photoinduced carriers. Recombination of the photoinduced electrons and holes was effectively inhibited during the photocatalytic process. Although this improved the photocatalytic activity of the samples, peak intensities and areas increased when the Fe^{3+} doping content increased to 0.05 due to heavy Fe doping— doping ions became recombination centers of electrons and holes; therefore, the PL intensities and areas of STO_3 were higher than those of STO_2.
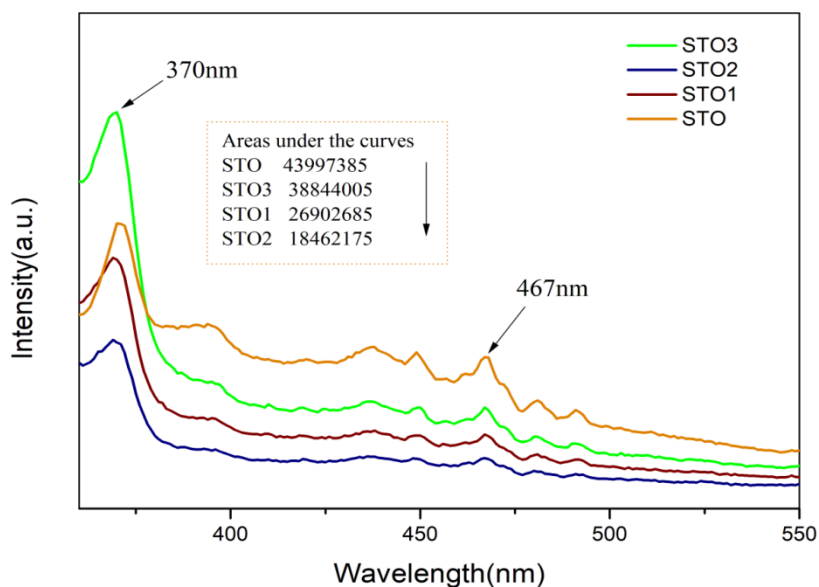
Figure 5. PL spectra of STO, STO2, STO4, and STO5 samples.

UV–vis DRS was then used to investigate the optical properties of the samples. Figure 6 shows the DRS spectra of all samples. According to the spectra, the visible light absorption of pure strontium titanate (STO) was negligible and nearly zero; however, there were obvious absorption edges around 400-800 nm for all the Y-Fe co-doped samples. This result indicated that $Y_{0.03}Sr_{0.97}Ti_{1-x}Fe_xO_{3-\delta}$ (x =0.03, 0.04, 0.05) was useful as a visible light catalyst.
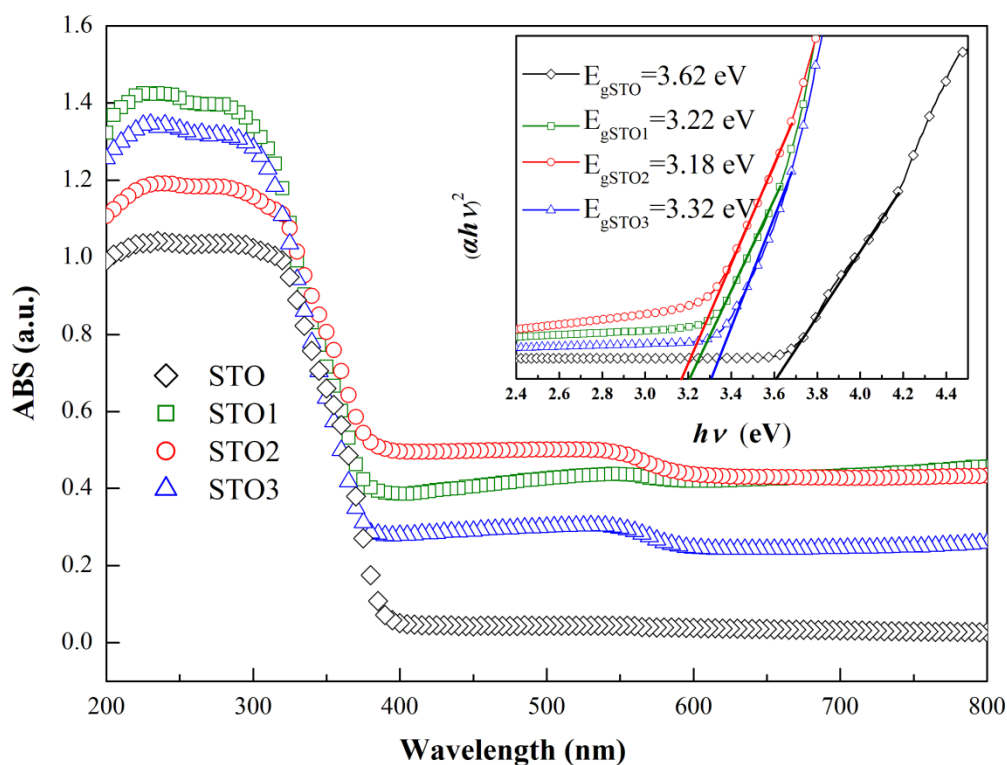

Figure 6. DRS spectra and Tauc plots (inset) for pure STO and Y-Fe co-doped STO samples.

The Tauc curves of samples are shown in Figure 6. The band gap value of the STO sample was 3.62 eV. The band gap values of STO_1, STO_2, and STO_3 were 3.22, 3.18, and 3.32 eV, respectively. Notably, the Eg value gradually reduced with increasing doped Fe. However, when the doped Fe^{3+} increased to 0.05, the Eg value increased.

This result might be due to several reasons. First, the ionic radius of Y is close to Sr, and that of Fe is close to Ti; given this, co-doped Y and Fe allow for Y^{3+} to dope into the Sr-site and In^{3+} into the Ti-site. This forms impurity energy levels, thus decreasing the band gap value [25]. Second, there is an excitation for 3^d electron of Fe^{3+} to the STO conduction band during charge transfer transition [26]. The charge transfer transition is between Fe ions ($Fe^{3+} + Fe^{3+} \rightarrow Fe^{4+} + Fe^{2+}$) [27].

XPS was then used to further explore the surface chemical composition and valence state of STO_2 sample. Results are shown in Figure 7, which confirmed the existence of Fe2p, Fe3p, O1s, Ti2p, Ti3p, Sr3s, Sr3P, and Sr3d in the XPS survey spectrum of the STO_2 sample. The C1s signal (284.92 eV) was owing to energy calibration of the elements binding together.

Figure 7 (b-e) shows the high-resolution Fe2p, Y3d, Ti2p, and Sr3d and spectra (fit using a Gaussian method). In the Sr3d spectrum, Spinorbit of Sr3d was split into Sr 3d 3/2 and Sr 3d 5/2, with binding energies of 133.55 eV and 135.52 eV, respectively, indicative of the existence of Sr^{2+} in STO_2. The Ti2p spectra, which are centered at 458.08 eV and 464.05 eV, respectively, confirmed the existence of Ti^{3+} and Ti^{4+} in the STO_2 structure. Two peaks were still be observed in the Y3d spectrum with binding energies corresponding to 159.2 eV and 168.8 eV, where Y ions had a (+3) valance. Two peaks, the characteristics of Fe 2p1/2 (724.93 eV) and Fe2p3/2 (709.87 eV), were observed in the Fe2p spectrum. Taken together, the highresolution spectra of Y 3d and Fe2p showed that both Y and Fe ions had been successfully co-doped into the $SrTiO_3$ lattice.
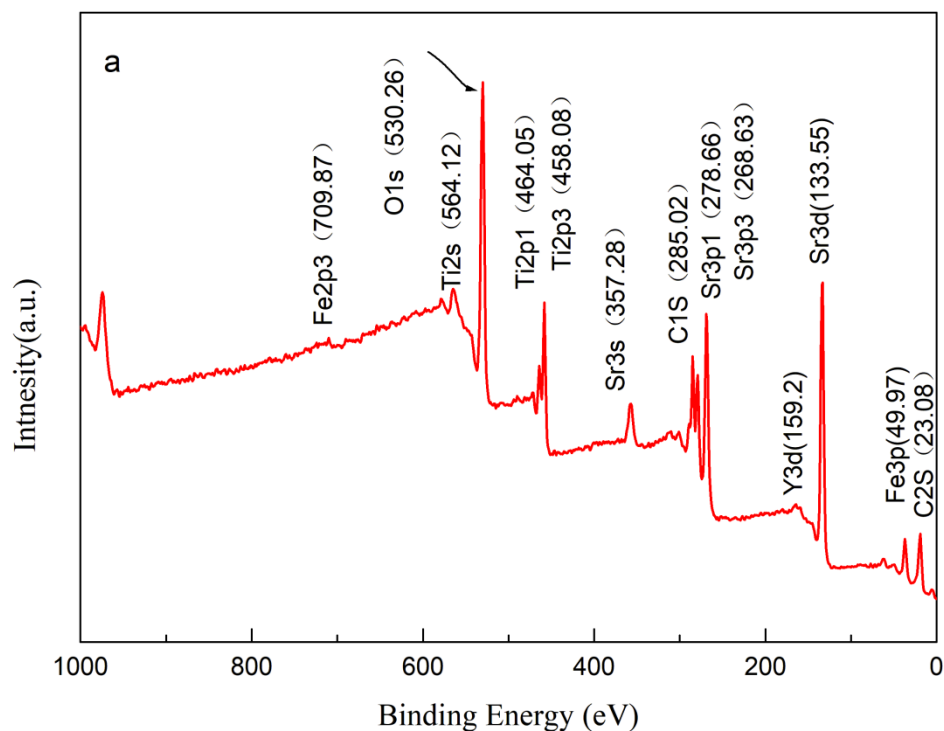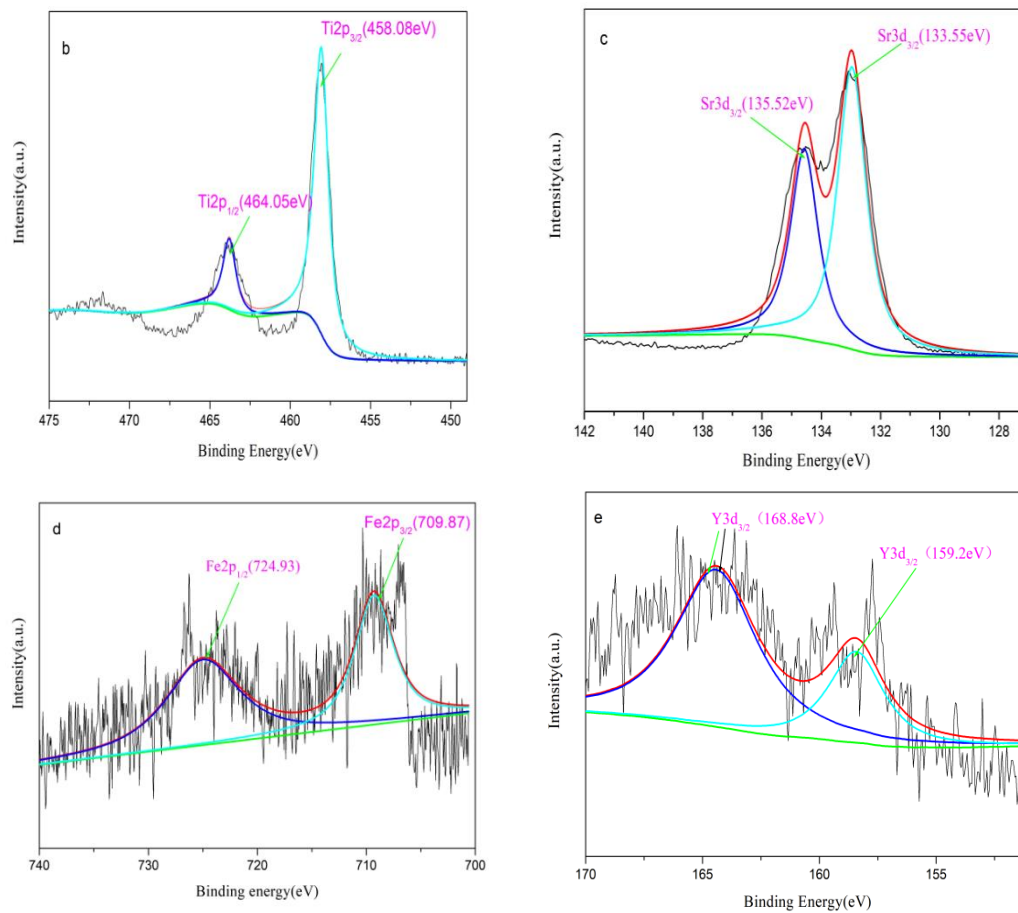
Figure 7. (a) XPS survey spectra, (b) Sr 3d XPS spectra, (c) Ti 2p XPS spectra, (d) Fe 2p XPS spectra, and (e) Y3d XPS spectra of the STO_2 sample.

The VB and CB edge positions of all samples were estimated as follows:

$$E_{CB}=X-E_e - E_g/2 \qquad (5)$$
$$E_{VB}=E_{CB}+E_g \qquad (6)$$

Where Ee is the energy of free electrons versus hydrogen, 4.5 eV; X, E_{CB}, and E_{VB} are semiconductor electronegativity, the potentials of CB and VB, respectively. Figure 8 shows the VB and CB potentials of the samples. For pure STO, the estimated CB edge potential versus NHE was -1.36 eV. After doping, the CB edge for STO_2 became -1.12 eV. For pure STO, the VB edge was 2.26 eV. In contrast, by doping, the CB edge for STO_2 became 2.06 eV.

There are three key factors related to the electronic structure of a photocatalyst material, which significantly contribute to its photocatalytic activity [6, 28, 29] These factors are as follows: (i) more positive VB edge which is compared with the redox potential of $OH^{\cdot}/OH^{-}$ (1.99 eV); (ii) a narrow bandgap helps enhance the light absorption ability; (iii) more negative CB edge compared to the redox potential of $O_2/O_2^{\cdot-}$ (-0.33eV). Together, these are beneficial to forming the $OH^{\cdot}$ radical. In order to achieve a best photocatalytic behavior, balance between the three factors mentioned above is critical.
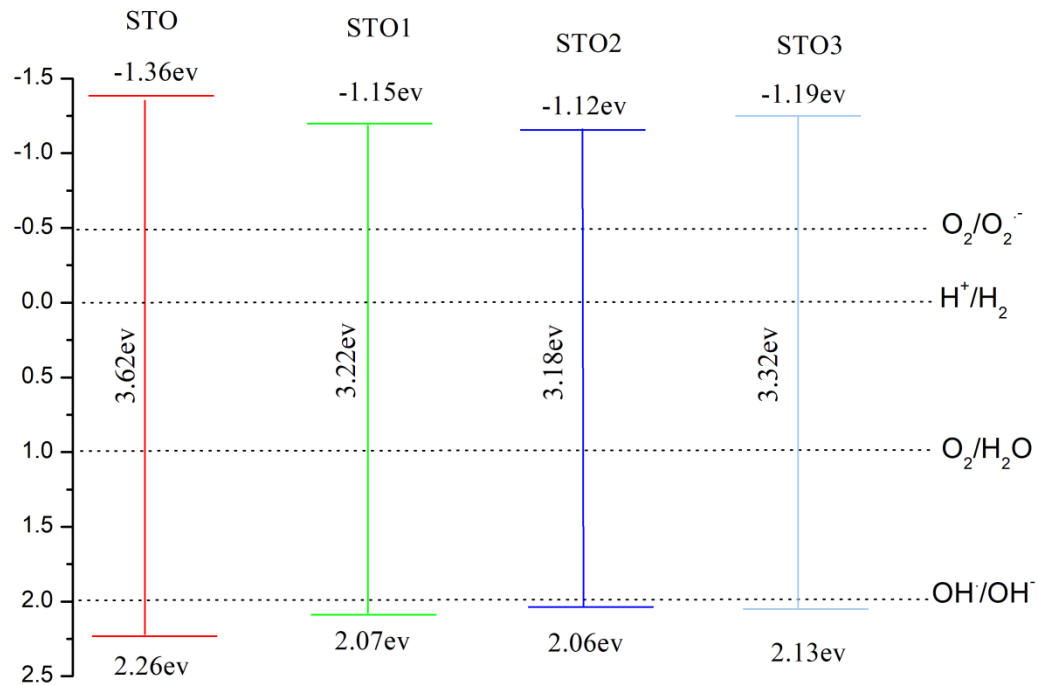
Figure 8. The calculated CB and VB edge potentials for all samples.
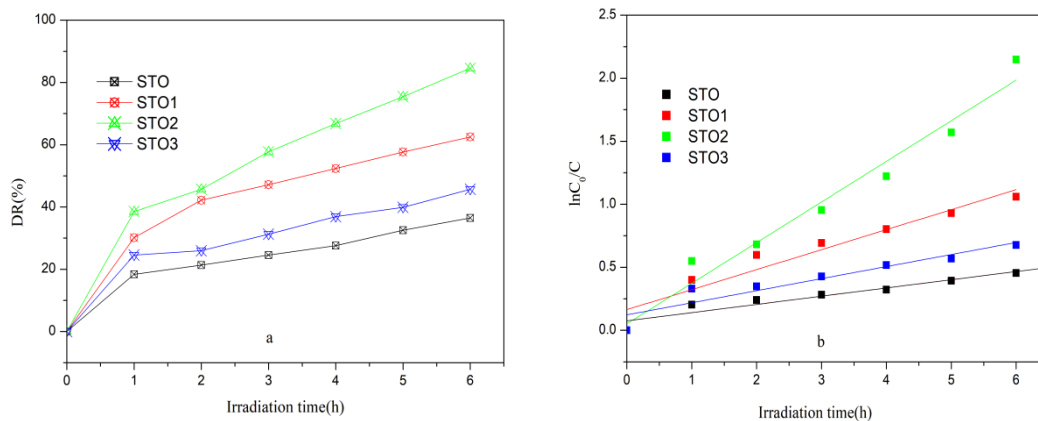
Figure 9. (a) Time dependence of C_0/C for MO photodegradation of the STO_2 sample. (b) Effect of different catalyst doses on MO degradation degree

We next examined the photocatalytic activity of samples by analyzing the methyl orange (MO) degradation under visible light irradiation. Figure 9 (a) indicates the effect of Y-Fe co-doping on the degradation degree (DR) of MO dye across all samples. Table 1 shows the DR values of MO for all samples after 6 h. When the catalyst was not present, MO degradation efficiency was low and effectively negligible. As indicated, Y- and Fe-co-doped samples had greater catalytic efficiency, with photodegradation efficiency increased with increasing Fe doping. More specifically, the STO degradation degree was the lowest (36%) and DR increased from 62 to 84% with increasing doping concentration from 0.02 to 0.05. This may be caused by increased oxygen vacancy with increasing

doped Fe. Oxygen vacancy increased with increasing Fe content according to Equation (7). Moreover, the combination of increased oxygen vacancy with the photogenerated electron (e⁻) in the conduction band effectively prevented the recombination of photogenerated electron (e⁻) and photogenerated hole (h⁺), thereby improving the overall catalytic activity.

$$Fe_2O_3 \rightarrow 2Fe'_{Ti^{4+}} + V_O^{\bullet\bullet} + 3O_o^{\times} + \frac{1}{2}O_2$$

$$(7)$$
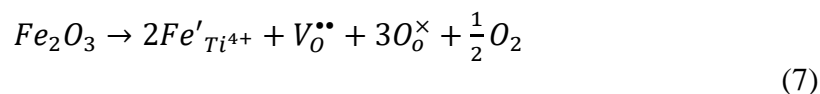
However, when the doped Fe^{3+} increased to 0.05, the photodegradation efficiency decreased due to extra doping ions became recombination centers of holes and electrons, consistent with the PL results.

Equation 8 was used to investigate the photocatalytic degradation kinetics and quantify the photodegradation degree :

$$\ln(\frac{C}{C0}) = -Kt$$

$$(8)$$

Where t is the irradiation time and K is the apparent rate constant. As shown in Equation 8 and Figure 9 (b), there was a linear relationship between the reaction time (t) and $\ln(C_0/C)$, suggesting the reaction is pseudo-first-order. Table 1 shows the values of kinetic on the degradation of MO dye across samples. Generally speaking, high values of the regression coefficient (R2) indicate the degradation mechanism follows first order kinetics [30, 31]. The STO_2 sample exhibited a higher activity with a rate constant of k=0.3223 min^{-1}, consistent with a better photocatalytic performance for MO degradation.

Table 1. DR and kinetic values for the degradation of MO dye by different samples.

sample	DR (%)	K (min^{-1})	R^2
STO	36	0.0652	0.9132
STO1	62	0.0957	0.9238
STO2	84	0.3223	0.9709
STO3	46	0.1586	0.8934

The mechanism behind STO_2 photocatalysis is next described. First, MO was adsorbed onto the STO_2 when in the water. With visible light radiation, electron and hole pairs occurred. In STO_2, both CB and VB were positioned at -1.12 eV and 2.06 (versus NHE), respectively. Since the CB position was more negative than the redox potential of $O_2/O^{\cdot-}$ (-0.33 eV), after reacting with O_2, the CB photo-generated electrons produced O_2. Since the CB position was more negative than the redox potential of

$O_2/O^{.-}$ (-0.33 eV). The reaction between these electrons and H_2O_2 generated $OH^.$ radicals, resulting in rapid oxidation of MO.

Furthermore, the VB photosynthetic holes are also involved in the direct oxidation of MO due to its higher oxidation potential. Meanwhile, the hole reacts with OH to produce OH radicals that oxidize water. Thus, the easy degradation of MO to less harmful minerals is partly due to the formation of reactive oxygen species (O_2 and OH).

4. CONCLUSION

Currently, doped $SrTiO_3$ catalysis materials are limited to N-doped, Fe-doped [32, 33] and La and Fe co-dopeds. the reports about Y and Fe co-dopeds $SrTiO_3$-based materials used as the Visible Light Photocatalysts are incomplete. In this paper, $Y_{0.03}Sr_{0.97}Ti_{1-x}Fe_xO_{3-\delta}$ (x = 0.03, 0.04, 0.05) were successfully prepared using the sol-gel method. The effects of different doping amounts on the morphological, optical, structural, and photocatalytic properties of $SrTiO_3$ were investigated. As a function of the doping process, the main crystalline phase of $Y_{0.03}Sr_{0.97}Ti_{1-x}Fe_xO_{3-\delta}$ perovskite structure was demonstrated to have a decreased average crystallite and particle size of $SrTiO_3$. Moreover, the BET surface area increased to 23.5 m^2/g after the doping process and visible light absorption of $Y_{0.03}Sr_{0.97}Ti_{1-x}Fe_xO_{3-\delta}$ (x = 0.03, 0.04, 0.05) was increased. Finally, the band edge was evidently moved to a longer wavelength. In summary, $Y_{0.03}Sr_{0.97}Ti_{0.96}Fe_{0.04}O_{3-\delta}$ was obtained with optimal doping elements and exhibited a highperformance photocatalytic activity of 84% degradation efficiency, with a 48% higher highperformance photocatalytic activity over pure strontium titanate. Lijuan Chen et al. [32] used N-doped strontium titanate to degrade MO, only 18% higher than pure strontium titanate, and the enhanced photocatalytic activity may be attributed to the binding of increased oxygen vacancy to photogenic electrons (e-), effectively preventing the recombination of photogenic electrons (e-) and photogenerated hole (h^+). M. Abdi et al used La-Fe co-doped $SrTiO_3$ titanate to degrade MO, Left in optimal conditions,the MO solution was degraded by 96% after 3 h illumination.however,it is complicated to prepare the La-Fe co-doped photocatalyst.In a word, the prepared sample ($Y_{0.03}Sr_{0.97}Ti_{1-x}Fe_xO_{3-\delta}$) is a visible photocatalyst and is a promising candidate for the degradation of organic pollutants.

AUTHORSHIP CONTRIBUTION STATEMENT
Jing Wang: Contributed to the methodology, conceptualization, and draft of manuscript. Nan Li: Contributed to experimental resources and data analysis.
Yunlong He: Contributed to experimental resources and data analysis. Yanhua Tang: Assisted in manuscript revision. Ke Shan: Assisted in manuscript revision.

DECLARATION OF COMPETING INTERESTS
The authors declare that they have no competing interests.

References

1. C. Zhou and C. Lai, *J. Appl. Catal.*, 238(2018)6.
2. K. Yu, C. X. Zhang and YChang, *J. Appl. Catal.*, 200(2017)514.
3. N. CH, C. C.Fu and R.S. Juang, J. *Clean. prod.*, 202(2018)413.
4. H. Nguyen, C. C. Fu and R. S, *J. Clean. prod.*, 413(2018)202.
5. Y. T. Xu, and D. D. Yuan, *J. Mater Chem A.*, 6(2018)13359.
6. H. M. Joseph, S. Sugunan, L. Gurrala, M. K.Mohan and S.Gopi, *J. Ceram. int.*, 8842(2019)30879.
7. H. Kisch,. J. *John Wiley & Sons.,* 2015.
8. A. Mills, C. O'Rourke and K.Moore, *J. Photochem. Photobiol. Chem.*, 310 (2015)66.
9. R. Sivasamy, P. Venugopa and R.Espinoza-Gonzalez, *J. Ceram. Int.*, 262(2019)0272.
10. T.B. Wermuth, S. Arcaro, J.Venturini and T.M. H. Ribeiro, *J. Ceram. Int.*, 45(2019)24137.
11. K. Shan and Z. Yi, *J. Dalton Trans.*, 49(2020) 6682.
12. A. Rothschild, S. J. Litzelman, H. L. Tuller, W. Menesklou, T. Schneider and E. I.Tiffee, *J. Sens. Actuators B.*, 108(2005) 223.
13. K. Shan, and Z. Yi, *J.Scr. Mater.*, 107(2015) 119.
14. C. Luo, J. Ji, J. Yue, Y. Rao, G.Yao , D. Li ,Y. Zeng, R. Li, L. Xiao, X. Liu, J.Yao, and F. Ling, *J. Opt. Mater.*, 60(2016)383.
15. M. Makarova, A.Dejneka, J. Franc, J. Drahokoupil, L. Jastrabik and V. Trepakov, *J. Opt. Mater.*, 32(2010)803
16. D. Eagles, *J. Phys.B Condens. Matter.*, 457(2015)172.
17. J. Denis, V.Vladislav and A. Alekse, *J. Am. Ceram. Soc.*, 94**(**2011)2993.
18. K. Attaphol , H. Sitchai and S. Ekaphan, *J. Microelectron. Eng.*, 126(2014)42.
19. Z.Wei, H. Li and W.Pan, *J. Mater. Sci.*, 47(2012)8216.
20. J.Dawson, H.Chen and I.Tanaka, *J. Phys. Chem. C.*, 118(2014)14485.
21. J. Xu, Y.Wei and Y. Huang, *J. Int.*, 40(2014)10583.
22. D. Saadetnejad and R. Yildirim *J. ICpes.*, 43(2018)1116.
23. Z. Xin, J.Shi and C.Li, *J. Phys. Chem. C.*, 115(2011)8305.
24. M. Abdi and V. Mahdikha, *J.optmat.*, 83(2020)109803.
25. K. Shan, Yi, Z. Z and Wang. J, *J. Nano Res.*, 11(2021)3379.
26. Z. Zhao, Q. Liu. *J.Phys. D Appl. Phys.*, 41(2008)085417.
27. J. Zhu, F.Chen, J.Zhang, H.Chen, M. Anpo, *J. Chem.*, 180(2006)196.
28. A. Nakaruk ,C. Lin, C.Koshy, C. Sorrell, *J.Adv. Appl. Ceram.*, 111(2012)129.
29. M. Sundararajan, L. John Kennedy, P. Nithya, J. Judith Vijaya and M. Bououdina, *J. Phys. Chem. Solid.*, 108 (2017)6.
30. M. Sundararajan, V. Sailaja, L. John Kennedy, J. Judith Vijaya, *J. Ceram. Int.*, 43 (2017) 540.
31. B. I. Kharisov, H.V.R. Dias and O.V. Kharissova, *J. Chem.*, 12(2019)1234.
32. 31.U.G. Akpan and B.H. Hameed, *J. Hazard Mater*. 170(2009)520.
33. I. Atkinson, V. Parvulescu, and J.Pandele Cusu, *J.Photobiology A:Chemistry.*, 368(2019)41.